Stellar X-ray activity and habitability revealed by *ROSAT* sky survey

Henggeng Han,[1] Song Wang[†],[1, 2] Chuanjie Zheng,[1, 3] Xue Li,[1, 3] Kai Xiao,[3] and Jifeng Liu[1, 3, 2, 4]

[1]*Key Laboratory of Optical Astronomy, National Astronomical Observatories, Chinese Academy of Sciences, Beijing 100101, People's Republic of China*
[2]*Institue for Frontiers in Astronomy and Astrophysics, Beijing Normal University, Beijing, 102206, People's Republic of China*
[3]*School of Astronomy and Space Science, University of Chinese Academy of Sciences, Beijing 100049, People's Republic of China*
[4]*New Cornerstone Science Laboratory, National Astronomical Observatories, Chinese Academy of Scciences, Beijing, 100012, People's Republic of China*

ABSTRACT

Using the homogeneous X-ray catalog from *ROSAT* observations, we conducted a comprehensive investigation into stellar X-ray activity-rotation relations for both single and binary stars. Generally, the relation for single stars consists of two distinct regions: a weak decay region, indicating a continued dependence of the magnetic dynamo on stellar rotation rather than a saturation regime with constant activity, and a rapid decay region, where X-ray activity is strongly correlated with the Rossby number. Detailed analysis reveals more fine structures within the relation: in the extremely fast rotating regime, a decrease in X-ray activity was observed with increasing rotation rate, referred to as super-saturation, while in the extremely slow rotating region, the relation flattens, mainly due to the scattering of F stars. This scattering may result from intrinsic variability in stellar activities over one stellar cycle or the presence of different dynamo mechanisms. Binaries exhibit a similar relation to that of single stars while the limited sample size prevented the identification of fine structures in the relation for binaries. We calculated the mass loss rates of planetary atmosphere triggered by X-ray emissions from host stars. Our findings indicate that for an Earth-like planet within the stellar habitable zone, it would easily lose its entire primordial H/He envelope (equating to about 1% of the planetary mass).

Unified Astronomy Thesaurus concepts: Habitable zone (696); Late-type stars (909); Stellar activity (1580); Stellar rotation (1629); X-ray stars (1823)

1. INTRODUCTION

The mechanism responsible for coronal heating has long been a widely discussed subject. Corresponding theories includes the dissipation of Alfvén waves (e.g. Alfvén 1947; van Ballegooijen et al. 2011) or impulsive energy release due to the dissipation of magnetic stress of bipolar fields, i.e., the *nanoflare* model (Parker 1988). X-ray emission, also named X-ray activity, has been detected on most stars throughout the Hertzsprung-Russell diagram (HRD). For low-mass stars the X-ray activity originates from hot plasma in the corona (Vaiana et al. 1981), which is strongly related to stellar magnetic fields. Therefore, investigating stellar magnetic activity could provide valuable insights into the mechanism behind coronal heating.

Stellar rotation and differential rotation are two key ingredients in stellar dynamo theories (e.g. Parker 1955). Generally, stellar activity proxies, including Ca II H&K lines (e.g. Noyes et al. 1984; Mittag et al. 2018), Hα lines (e.g. Newton et al. 2017; Han et al. 2023) and X-ray emissions (e.g. Pizzolato et al. 2003; Wright et al. 2011), are strongly correlated to stellar rotation. The consequent stellar activity-rotation relation has been extensively explored from various perspectives, which is expected to shed light on the magnetic dynamos operating on different stars. In general, the stellar activity-rotation relation is divided into two regions, i.e., the saturated region, in which the stellar activity level keeps constant and the decay region, in which activity level is dependent on stellar Rossby number($P_{\rm rot}/\tau$) (e.g. Noyes et al. 1984). Interestingly, for both dwarfs and giants, which develop different stellar structures, the decay regions of activity-rotation relation obey the same power-

law, indicating the development of the same turbulence-related dynamo (Lehtinen et al. 2020).

However, such classical picture may not be universal. In the decay region of the X-ray activity-rotation relation, F-type stars exhibit a possibly different power-law (Pizzocaro et al. 2019) compared with other type stars. Similar phenomenon was also found with the Hα proxy for F stars (Han et al. 2023). A revising of the X-ray and Ca II H&K activity-rotation relation shows that a single power-law could not describe the decay region properly (Mittag et al. 2018). All these studies suggest that different types of stars may develop different dynamos, which could be revealed by the different slopes in the decay region.

Another hot topic regarding on stellar activity is its influence on planetary habitability. The continuous habitable zone (CHZ) is the region in which liquid water could be maintained on the surface of a planet (e.g. Kopparapu et al. 2013). However, planets in CHZ may still be inhabitable due to strong high energy radiation, including UV and X-ray emissions from their host stars. High energy radiation of host stars plays an important role in stripping planetary atmosphere (e.g. Lammer et al. 2009), while the composition of planetary atmosphere determines the temperature and pressure of a planet and thus the capability of generating life (Kite & Barnett 2020; Swain et al. 2021). Hence, it is necessary to study the potential impacts of stellar activities on the habitability of planets.

In this work, we constructed a homogeneous X-ray sample with stellar parameters using *ROSAT* 2RXS catalog together with LAMOST DR10, APOGEE DR16 and Gaia eDR3. Combined with various catalogs of photometric sky surveys, we investigated statistic properties of stellar X-ray activity and its influence on stellar habitable zone. Structure of this paper is as follows. In Section 2 we described our sample construction, target classification and cleaning processes. In Section 3 we discussed the X-ray activity distributions and the activity-rotation relations in detail. A discussion on the Ultraluminous sample is given in Section 4. In Section 5 we studied the impacts of X-ray emission on planetary atmosphere. In Section 6 we presented a brief summery.

2. TARGETS SELECTION AND CLASSIFICATION

2.1. *Targets selection*

The ROentgen SATellite (*ROSAT*) was designed to carry out all sky X-ray survey with high sensitivity in energy band of 0.1–2.4 keV (Truemper 1982). Consisting of the bright source catalogue and the faint source catalogue, the *ROSAT* 1RXS catalogue contains roughly 127,730 sources (Voges et al. 1999). Later on, the
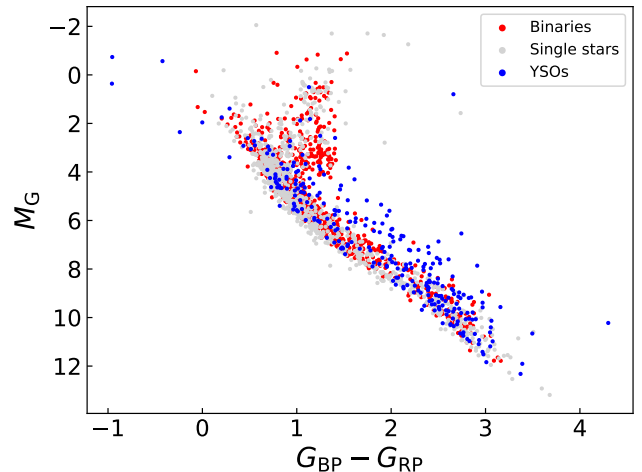

Figure 1. Colour-magnitude diagram of our sample. Single stars, binaries and YSOs are shown with grey, red and blue points, respectively.

ROSAT point source catalogue underwent a renewal and was named as the Second *ROSAT* All-Sky Survey Point Source Catalog(RASS2RXS), which contains 135,000 X-ray sources (Boller et al. 2016). In this study, we used the *ROSAT* 2RXS catalogue.

Recent spectroscopic surveys have provided tens of millions of stellar spectra, which can be used to derive stellar atmospheric parameters. For example, the LAMOST DR10 low-resolution catalogue contains over 10 millions of spectra of A-, F-, G-, K- and M-type stars (Cui et al. 2012; Luo et al. 2015), while the Apache Point Observatory Galactic Evolution Experiment (APOGEE)-2 project has released 473,307 spectra of 437,445 stars (Jönsson et al. 2020).

Due to the poor positional accuracy of the *ROSAT* 2RXS catalog, we first cross-matched the *ROSAT* 2RXS catalogue with LAMOST DR10 and APOGEE DR16 datasets using TOPCAT[1] with a radius of 10". The stellar parameters were extracted from the spectra with the highest signal to noise ratio. Then the sample was cross-matched with Gaia eDR3 (Gaia Collaboration et al. 2021) and its distance catalog (Bailer-Jones et al. 2021), with a radius of 3", in order to derive stellar parallaxes, distances and Gaia magnitudes. To ensure the reliability of distances, only targets within 5 kpc with a relative parallax error (calculated as the parallax error divided by parallax) smaller than 0.2 were remained. We derived an initial sample containing 2085 targets with X-ray emission and stellar parameters.

---

[1] http://www.star.bris.ac.uk/%7Embt/topcat

Table 1. Stellar parameters of each target in our sample.

Gaia ID	R.A. (degree)	Decl. (degree)	$T_{\rm eff}$ (K)	$\log g$ (dex)	[Fe/H] (dex)	Distance (pc)	Radius ($R_\odot$)	Type
(1)	(2)	(3)	(4)	(5)	(6)	(7)	(8)	(9)
158364034415872	45.540909	0.77053	3636±81	5.03±0.16	-0.32±0.21	371±12	0.49±0.03	Dwarf
7798908990819968	46.445812	7.760454	6605±18	4.17±0.02	0.1±0.01	284±13	2.08±0.16	Dwarf
9124679495764864	50.91339	5.687451	3131±105	4.44±0.24	-0.19±0.32	37±1	0.49±0.02	YSO
9770058461712000	52.784938	7.223575	5039±57	4.38±0.08	0.04±0.04	100±1	1.05±0.08	Binary
9964981257351936	51.278631	7.393461	6052±127	4.2±0.08	0.05±0.01	127±1	1.31±0.03	Binary
17644790803959552	51.831128	13.365846	4965±33	4.42±0.05	-0.05±0.03	200±1	1.08±0.04	Binary
18211043587721088	40.357975	5.9884	4073±58	4.14±0.07	-0.33±0.03	44±1	1.0±0.02	Dwarf
20896222781456768	43.810399	9.111804	6062±20	4.36±0.02	0.15±0.01	146±1	1.27±0.08	Dwarf
24331990460013568	36.354505	10.464996	5384±56	4.36±0.08	0.42±0.05	371±2	0.94±0.07	Binary
27487726270657536	45.346629	11.396368	3930±66	5.03±0.14	-0.47±0.2	65±1	1.09±0.13	YSO
29835488537920768	47.791111	14.403983	6313±13	4.11±0.02	-0.1±0.01	327±2	1.65±0.01	Dwarf
...	...	...	...	...	...	...	...	...

(1) Gaia ID: Gaia eDR3 source ID. (2) R.A.: right ascension (3) Decl.: declination. (4) $T_{\rm eff}$: effective temperature. (5) $\log g$: surface gravity. (6) [Fe/H]: metallicity. (7) Distance: Gaia distance. (8) Radius : stellar radius. (9) Type: stellar types

When cross-matching an X-ray catalog with optical catalogs, the standard approach is to identify the nearest optical target (to the X-ray spatial position) as the counterpart of a X-ray source. Due to the poor position uncertainty of *ROSAT* sources, it is necessary to verify the accuracy of the cross-match process and the false match rate of the optical counterparts.

Considering the high positional accuracy of *Chandra* observations, the false match rate between *Chandra* and optical catalogs using the nearest counterparts could be low. Here we used the *Chandra* sources to roughly estimate the false match rate of this study. we cross-matched the *ROSAT* 2RXS catalog and the *Chandra* point source catalog (Wang et al. 2016). For each *ROSAT* target, all *Chandra* counterparts within a 10" radius were picked out. Two selection criteria were applied: (1) selecting the nearest *Chandra* targets and (2) selecting the brightest *Chandra* targets. Here we assumed the brightest *Chandra* target is the true counterpart. This process returned 854 matches, with 775 being identical sources (i.e., the nearest target is also the brightest). Consequently, the false match rate is approximately 9% (=79/854). Furthermore, when these two catalogs were cross-matched using radii of 20" and 30", the false match rates are about 11% (=183/1613) and 14% (=302/2086), respectively. Therefore, in our sample, approximately 10% of the optical counterparts to *ROSAT* sources may be incorrectly identified.

2.2. *Target classification and cleaning*

After the sample construction, the most important process is target classification and cleaning. To determine the variable types in our sample, we first cross-matched it with various photometric catalogs, including: (1) periodic variable stars of the Catalina surveys (CSS; Drake et al. 2014); (2) the ASAS-SN catalog of variable stars (e.g. Jayasinghe et al. 2020; Christy et al. 2022); (3) the ZTF variable star catalog (Chen et al. 2020); (4) the WISE variable star catalog (Chen et al. 2018); (5) rotating variables from the *Kepler* and K2 mission (McQuillan et al. 2014, 2013; Santos et al. 2019, 2021) and the third version of *Kepler* eclipsing binary catalog[2]; (6) the OLGE eclipsing and ellipsoidal binary catalog (Soszyński et al. 2016); (7) the general catalog of variable stars (GCVS; Samus' et al. 2017); (8) the Gaia variable sources catalog (Rimoldini et al. 2023). (9) two TESS eclipsing binary catalogs (Howard et al. 2022; Prša et al. 2022). For stars that are identified by multiple catalogs, we graded them according to photometric quality (i.e., *Kepler*, K2, TESS, ZTF, ASAS-SN, CSS, WISE, OLGE, AASVO, GCVS) and used this order to select the first priority classification. To further identify possible binaries in our sample, we collected radial velocity (RV) data from LAMOST and APOGEE catalogs. Targets exhibiting RV variations exceeding 20 km/s were considered to be spectroscopic binaries. Meanwhile, some double-lined spectroscopic binary (SB2) catalogs
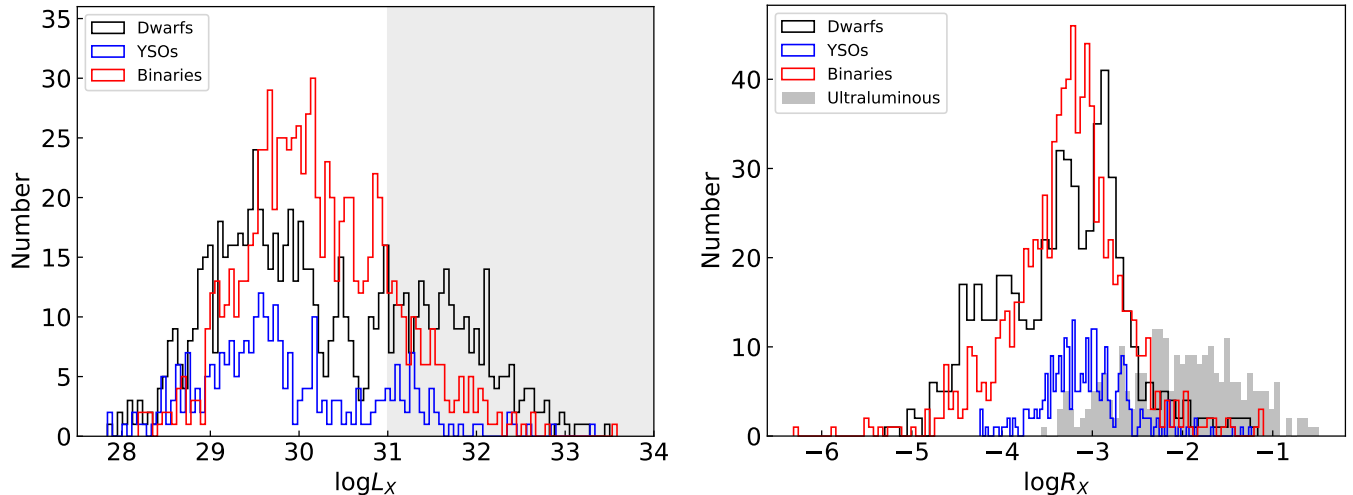
---

[2] http://keplerebs.villanova.edu

Figure 2. Panel (a): Histograms of L_X of dwarfs, giants, YSOs and binaries. Shaded area represents region in which X-ray luminosity is higher than 10^{31} erg/s. Panel (b): Histograms of R_X of dwarfs, giants, binaries and Ultraluminous sources.

have been given from LAMOST spectra (Li et al. 2021; Kovalev et al. 2022; Zhang et al. 2022) and APOGEE spectra (Kounkel et al. 2021). In addition, astrometric binaries were selected based on the catalog of El-Badry et al. (2021).

Young stellar objects (YSOs) usually exhibit strong X-ray emission (Favata et al. 2003) which is unrelated to stellar magnetic dynamo (Flaccomio et al. 2003; Preibisch & Feigelson 2005). To classify YSOs from our sample, we cross-matched our dataset with YSO catalogs (Marton et al. 2016, 2019, 2023) using a radius of 3". Among the potential YSOs identified by Marton et al. (2019), only those with a reliability exceeding 90% were selected. Meanwhile, YSOs that are flagged by SIMBAD were used as supplement.

Finally, we removed some contamination from our sample. By cross-matching with SIMBAD, objects flagged with Galaxy, QSO, symbiotic stars, high mass X-ray binaries, low mass X-ray binaries and cataclysmic variables were removed. Binary containing white dwarfs were further excluded based on catalogs from Ren et al. (2018, 2020) and El-Badry et al. (2021). We also checked the DSS image of each target to avoid the contamination from nebulae and star formation regions.

Figure 1 shows the colour-magnitude diagram of the final sample, including 821 dwarfs, 73 giants, 872 binaries and 276 YSOs. In this work, single stars with $\log g$ higher than 3.5 were classified as dwarfs and giants are those with $\log g$ smaller than 3.5. Stellar parameters of the final sample are listed in Table 1.

2.3. *Comparison with previous catalogs*

Based on a Bayesian method, Salvato et al. (2018) presented a catalog of ALLWISE and Gaia counter-

parts of *ROSAT* 2RXS targets with Galactic latitudes of $|b| > 15°$, offering us an ideal catalog to cross-check our sample. Out of 1589 common X-ray sources, 1440 have the same optical counterparts, leading to a coincidence rate of ≈90%. This further confirms the acceptability of the optical counterparts identification in our sample.

3. X-RAY ACTIVITIES AND STELLAR ROTATION

3.1. ROSAT *X-ray fluxes*

Based on the Interactive Multi-Mission Simulator (PIMMS)[3], *ROSAT* count rate was converted into unabsorbed X-ray flux using the Astrophysical Plasma Emission Code (APEC) model. The plasma temperature was set to be $\log T = 6.5$, considering that most of the targets exhibit plasma temperature between $\log T = 6$ and $\log T = 7$ (Wang et al. 2020). The metallicity was set to be half of the solar metallitiy. The galactic extinction was calculated as follows (Zhu et al. 2017),

$$N_{\mathrm{H}} = 2.19 \times 10^{21}~A_V = 6.79 \times 10^{21}~E(B-V). \quad (1)$$

The interstellar reddening $E(B - V)$ was obtained using the three-dimensional dust map (Green 2018) constructed by photometry from Pan-STARRS1 and 2MASS together with Gaia parallaxes (Green et al. 2019). For 484 sources without extinction estimation from the Pan-STARRS1 dust map, we used the SFD dust map (Schlegel et al. 1998) with $E(B - V) = 0.884 \times E(B - V)_{\mathrm{SFD}}$ as a complement.

3.2. *X-ray activity*

---

[3] https://heasarc.gsfc.nasa.gov/docs/software/tools/pimms.html
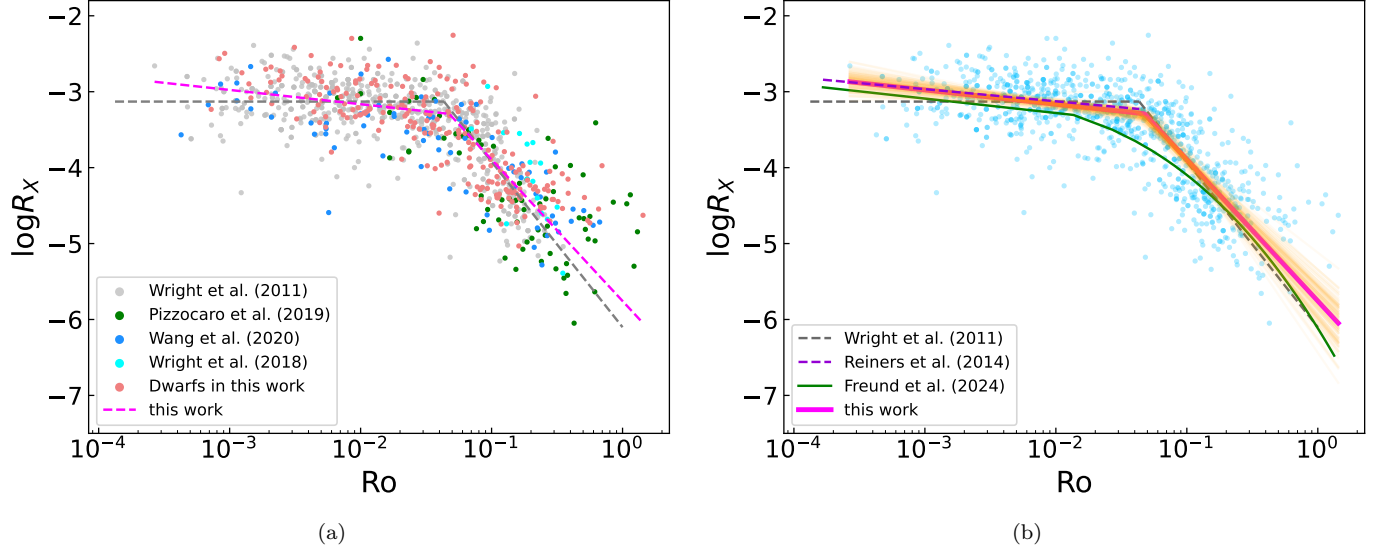
(a)

(b)

Figure 3. Panel (a): Activity-rotation relation of single stars. The grey, green, blue, cyan, and lightcoral dots are from Wright et al. (2011), Pizzocaro et al. (2019), Wang et al. (2020), Wright et al. (2018), and this study, respectively. Ro that were empirically estimated are shifted by a factor of Ro/3. The magenta lines are our best-fit results. Panel (b): Comparisons of activity-rotation relations from different studies. The shaded region shows 100 models extracted randomly from the posterior probability distribution.

The X-ray activity level is defined as

$$R_X = \frac{f_{X,\mathrm{sur}}}{f_{\mathrm{bol}}} = \frac{f_{X,\mathrm{obs}} \times (\frac{d}{R_\star})^2}{\sigma T_{\mathrm{eff}}^4}, \qquad (2)$$

where $f_{X,\mathrm{sur}}$ is the unabsorbed X-ray flux at the surface of stars and T_{eff} is the stellar effective temperatures. The stellar radius was calculated as $R_* = \sqrt{L_{\mathrm{bol}}/(4\pi\sigma T_{\mathrm{eff}}^4)}$, with the bolometric luminosity defined as $L_{\mathrm{bol}} = 10^{-0.4 \times (m_\lambda - 5\log_{10} d + 5 - A_\lambda + BC_\lambda - M_\odot)} L_\odot$. Here we used the apparent magnitudes in six bands including G, BP, RP, J, H, and K_{S}. m_λ is stellar apparent magnitude, and d is the Gaia eDR3 distance (Bailer-Jones et al. 2021). BC_λ is bolometric correction for each band calculated using the *isochrones* python package (Morton 2015), based on stellar effective temperatures, $\log g$ and metallicity. $M_\odot$ and $L_\odot$ are solar bolometric magnitude and luminosity, respectively. The extinction A_λ was calculated as $A_\lambda = R_\lambda E(B-V)$, with R_λ being the extinction coefficient estimated following Fitzpatrick (1999). The mean value and standard deviation of the radii calculated from six bands were used as the final radius and its error, respectively. Furthermore, the X-ray luminosity L_X was calculated following $L_X = 4\pi f_{X,\mathrm{obs}} d^2$. Errors of R_X were derived using a random sampling of R_X based on the errors of $f_{X,\mathrm{obs}}$, d, $R_\star$ and T_{eff}. Comparison of R_X of common targets between this work and Wright et al. (2011) are given in Figure A1, which shows good agreement.

Figure 2 (Panel a) shows the distributions of L_X for dwarfs, binaries, and YSOs. One notable feature is the

presence of some sources with $L_X > 10^{31}$ erg/s. Generally, the X-ray luminosity of single dwarfs ranges from 10^{27} to 10^{30} erg/s (Pizzolato et al. 2003). YSOs can exhibit enhanced X-ray emission with X-ray luminosities about 10 to 10^4 times higher than that of main-sequence stars (Feigelson & Kriss 1981; Feigelson et al. 2002); in our sample, most YSOs exhibit a luminosity range of about 10^{29} to 10^{31} erg/s, suggesting that the majority of YSOs are of class II/III types.

Binaries also present higher luminosities than dwarfs. For example, RS Canum Venaticorum(RS CVn) variables can reach X-ray luminosities ranging from 10^{30} to 10^{32} erg/s (Motch et al. 2010). Therefore, it's quite unusual that many single main-sequence stars have $L_X > 10^{31}$ erg/s, leading us to suspect that they may not be of stellar origin. We categorized them as the "Ultraluminous" population and excluded them from the dwarf samples. Their nature will be discussed in Section 4. Figure 2 (Panel b) shows the distributions of R_X for dwarfs, binaries, YSOs, and Ultraluminous sources. Note that most Ultraluminous sources have R_X values higher than -2.5, further evidencing that they are not stars. Most YSOs exhibit high R_X values around -3, while dwarfs and binaries show much wider R_X distributions ranging from -5 to -2.

3.3. *Rotation periods and Rossby number*

Rotation is one of the key ingredients in the generation of stellar magnetic field. In order to investigate the X-ray activity-rotation relation (Pizzolato et al. 2003;
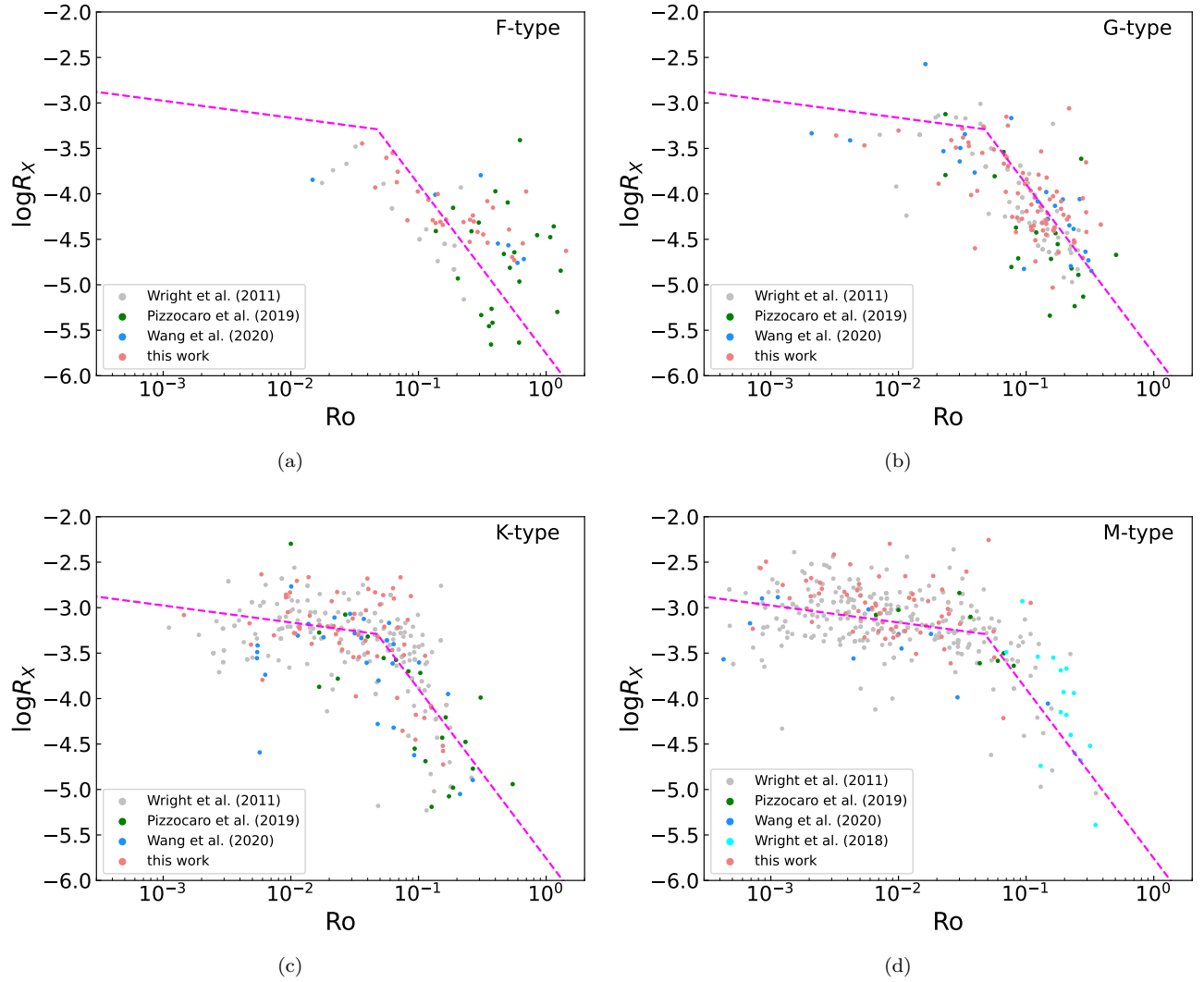
Figure 4. Activity-rotation relations of F-, G-, K-, and M-type single stars, respectively. Stars with T_{eff} lower than 4000 are classified as M-type stars. K-type stars are those with T_{eff} between 4000K and 5300K. G-type stars have T_{eff} ranging from 5300K to 6000K. T_{eff} range of F-type stars is set to be from 6000K to 7500K. Magenta dashed line is the best-fit activity-rotation relation shown in Figure 3.

Wright et al. 2011), it's necessary to build a sample with accurate rotating period measurements.

Through matching the catalogs mentioned in Section 2.2, periods are available for different types of variable stars, including rotation variables, RS CVn variables, and BY Dra variables. The TESS satellite has provided hundreds of thousands of stellar light curves, enabling the expansion of our rotational sample. We cross-matched our sample with the TESS input catalog (Stassun et al. 2019) and downloaded the PDC light curves provided by the TESS science processing operations center (SPOC) (Jenkins et al. 2016). TESS light curves used in this work can be found at MAST (MAST Team 2021; Ricker et al. 2015). For each target, the light curves from multiple sectors were combined for pe-

riod estimation using the Lomb-Scargle (LS) algorithm (Lomb 1976; Scargle 1982). Finally, the phase-folded light curves were visually checked to ensure reliable period estimation. Furthermore, pulsators were excluded by cross-matching the SIMBAD.

For close binaries, the orbital motion and rotation could be synchronized. For example, the variation of the light curves of BY Draconis (BY Dra) and RS CVn variables is dominated by the rotation of the late-type giant component, and the rotation periods equals to the orbital periods. For other binaries such as EA and EB types, the light curves are modulated by orbital motion.

The dimensionless parameter Ro, defined as $P_{\mathrm{rot}}/\tau_{\mathrm{c}}$, has been proved to be an appropriate quantity for investigating the stellar activity-rotation relation (Noyes

et al. 1984). τ_c is the convective turnover time, which was extracted from the Yale-Potsdam Stellar Isochrones (YAPSI; Spada et al. 2017). For each metallicity grid (i.e., [Fe/H] = +0.3, 0.0, −0.5, −1.0, −1.5), we selected the models within the errors of $T_{\rm eff}$ and log$g$, and calculated the median value of τ_c. For each star, the final τ_c value was determined by linear interpolation to the metallicity. The periods and τ_c are listed in Table 2.

3.4. Activity-rotation relation: "D^2" model

The relation between X-ray emission and stellar rotation has long been a hot topic. Pallavicini et al. (1981) found that for early-type stars, L_X is correlated with spectral type (i.e., stellar temperature), while for late-type stars, L_X is strongly proportional to stellar rotation velocity. Currently, the activity-rotation relation is described by a piece-wise model, including a saturated region where X-ray activity keeps unchanged and a decay region where X-ray activity is proportional to rotation period or Ro (e.g. Pizzolato et al. 2003; Mamajek & Hillenbrand 2008; Wright et al. 2011).

To investigate X-ray activity-rotation in a large sample, we collected objects with X-ray activity and Ro from previous literature, including (Wright et al. 2011, 2018; Pizzocaro et al. 2019; Wang et al. 2020). The R_X values from Wang et al. (2020) were converted into the energy band of 0.1–2.4 keV with PIMMS. For studies using empirical τ (e.g., Wright et al. 2011; Pizzocaro et al. 2019; Wright et al. 2018), their Ro values were shifted by Ro/3. In our sample, dwarfs with measured rotation periods have logL_X and logR_X ranges of from 28.02 to 30.93 and from -5.03 to -2.25, respectively. The large sample includes 1014 sources.

We applied a piece-wise power law model to fit the activity-rotation relation using the large sample (Figure 3) based on the *emcee* python package. It is widely used for Markov Chain Monte Carlo sampling (Foreman-Mackey et al. 2013). The model is described as follows,

$$\log R_X = \begin{cases} a + b\log{\rm Ro}, & \text{for Ro} \leq {\rm Ro_k} \\ a + (b-c)\log{\rm Ro_k} + c\log{\rm Ro}, & \text{for Ro} > {\rm Ro_k}, \end{cases}$$
(3)

where ${\rm Ro_k}$ represents the Ro value at the knee point separating the saturated and unsaturated regimes. Table 3 lists the best-fit parameters for single dwarfs, with the slopes being -0.19 in the fast rotating region, -1.86 in the slow rotating region and the break point being -1.32. Posterior distributions of parameters are given in Figure B1. We named the model consisting of two piece-wise power laws as a "D^2" model. This model includes a slow decaying part and a fast decay part, with the knee around Ro $\approx$ 0.047.

In contrast to Wright et al. (2011), our study reveals that in the classical saturation region, R_X continues to increase as stars rotate faster (i.e., in the first decay region of the "D^2" model), a trend which has also been noticed in previous studies (Reiners et al. 2014; Johnstone et al. 2021). Recently, based on the newly published *eROSITA* data, Freund et al. (2024) used a polynomial model to describe the activity-rotation relation, which also shows an increase of R_X in relation to the decreasing Ro (Figure 3). In order to examine the difference between the relations given by Freund et al. (2024) and other studies, we re-calculated the R_X values of Freund et al. (2024) using their catalog. Figure A2 shows a good agreement of R_X between these studies, suggesting the different relation presented by Freund et al. (2024) may be due to their estimation method of τ.

In the saturated regime, theoretical work has proposed that as a star rotates faster, the mixing length of a turbulent eddy will gradually grows until it reaches the depth of convective zone, which could lead to the saturation of magnetic energy (Wei 2022). However, fast rotating stars tend to be young stars, which could develop deeper convective zone. This would allow the continual growth of mixing length and thus the magnetic energy (towards younger ages). Reiners et al. (2014) suggested that the trend may be due to the remaining dependence of dynamo on rotation in this region or the scatter of X-ray luminosity of different stellar masses. Figure 4 shows that the saturation region is mainly occupied by K and M dwarfs. For both K and M dwarfs, especially M dwarfs, the decay trend can be clearly seen. This suggests the trend is most possibly due to a remaining dependence of magnetic dynamo on rotation, rather than a scatter of X-ray luminosities of different types of stars.

3.5. Fine structures in the activity-rotation relation: "SD^2F" model

Although the "D^2" model could generally describe the overall trends in the activity-rotation relation, there are still some fine structures in the low Ro region and high Ro region. We divided the sample into different bins of Ro, each containing 30 targets. We calculated the median value of R_X and the standard deviation for each bin. Figure 5 shows a decline of R_X when logRo is smaller than −2.7 and a significantly reduced slope when logRo is larger than −0.7. Therefore, the relation can be described by a "SD^2F" model, including one super-saturated region, two decay regions with different slopes and one flat region with almost constant Rx in the slow rotating regime.

Table 2. Derived stellar parameters of each target in our sample.

Gaia ID	$E(B-V)$	flux	R_X	τ_c	$P_{\rm rot}$
	(mag)	(erg/cm^{2}s)		(day)	(day)
(1)	(2)	(3)	(4)	(5)	(6)
158364034415872	0.08	9.70e-13±3.80e-13	1.10e-01±4.77e-02	-	-
7798908990819968	0.34	6.53e-13±3.22e-13	2.24e-04±1.23e-04	-	-
9124679495764864	0.01	1.71e-13±6.15e-14	3.68e-04±1.49e-04	-	-
9770058461712000	0.01	1.72e-12±1.74e-13	8.62e-04±1.71e-04	-	-
9964981257351936	0.01	2.15e-13±6.10e-14	5.21e-05±1.58e-05	14.68	1.25
17644790803959552	0.26	5.31e-13±2.63e-13	1.03e-03±5.20e-04	68.33	4.7
18211043587721088	0.01	3.50e-12±3.14e-13	8.54e-04±9.88e-05	142.31	4.48
20896222781456768	0.01	3.45e-13±1.06e-13	1.18e-04±4.07e-05	18.02	0.82
24331990460013568	0.1	6.45e-13±3.47e-13	4.17e-03±2.42e-03	-	-
27487726270657536	0.01	7.14e-13±1.05e-13	3.78e-04±1.19e-04	-	-
29835488537920768	0.17	1.56e-12±5.44e-13	1.33e-03±4.73e-04	-	-
...	...	...	...	...	...

(1) Gaia ID: Gaia eDR3 source ID. (2) $E(B-V)$: reddening. (3) flux: X-ray flux. (4) R_X: normalized X-ray luminosity. (5) τ_c: convective turnover time. (6) $P_{\rm rot}$: rotation period.

Table 3. Best-fit parameters of activity-rotation relations.

	a	b	c	Ro$_k$
Single stars	$-3.54^{+0.16}_{-0.15}$	$-0.19^{+0.07}_{-0.07}$	$-1.86^{+0.21}_{-0.21}$	$-1.32^{+0.06}_{-0.07}$
Binaries	$-3.75^{+0.34}_{-0.31}$	$-0.35^{+0.18}_{-0.17}$	$-2.07^{+0.25}_{-0.29}$	$-1.32^{+0.1}_{-0.1}$
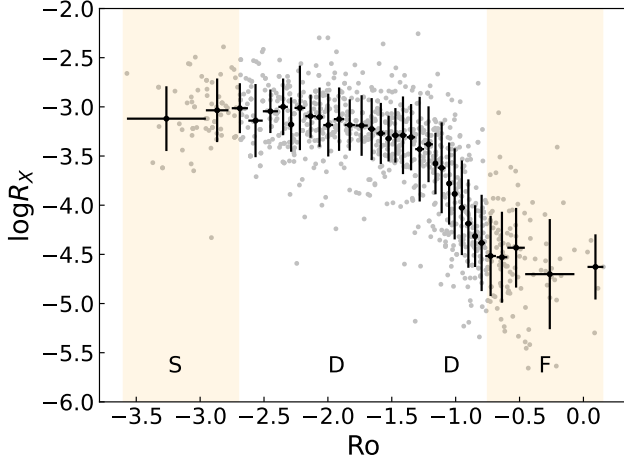
Figure 5. Fine structures of activity-rotation relation of single stars. "S" represents the super-saturation region. The first "D" represents the weak decay region while the second one corresponds to the fast decay region. "F" stands for the region with an almost flat slope.

In our study, the super-saturation is mainly caused by M stars. The super-saturation phenomenon has been observed in many previous studies on stellar X-ray activity (Randich et al. 1996; Stauffer et al. 1997; Wright et al. 2011) and still remains a topic of debate. Possible explanations include the decreasing of filling factor of active regions (Stępień et al. 2001) or the centrifugal stripping of stellar corona, which could result in the decreasing of X-ray emitting volume (James et al. 2000). Recently, our recent work has found some evidences of super-saturation with the $R'_{\rm HK}$ (Ding et al. in prep); Chahal et al. (2022) found a decline in the saturation value of $S_{\rm ph}$ index for BY Dra variables with short periods. The super-saturation observed in X-ray, chromospheric, and photospheric activity proxies would favor the scenario of the decrease in the filling factor of active regions as the mechanism for super-saturation.

The flat region (with high logRo) consists of F stars. The significantly reduced slope is caused by the scatter in R_X of F stars. Pizzocaro et al. (2019) suggested that among F stars, there may be unresolved active binaries contributing to additional (higher) X-ray activity. However, no similar scatter is observed for other types of stars. Meanwhile, Han et al. (2023) also noted a scat-

ter of $R'_{\mathrm{H}\alpha}$ for F and G stars in the high logRo regime, which can be attributed to the intrinsic variability of stellar activities. All the F dwarfs in this study and most F stars in Pizzocaro et al. (2019) have T_{eff} lower than 6500K, meaning that they are late-type F stars with thin convective zones and possibly rotation-related magnetic dynamos. It's worthy to investigate whether the scatter is caused by stars with a different dynamo.

3.6. *Activity-rotation relation of binaries*

Binaries show similar activity-rotation relation to single stars(Figure 6 and Figure 7). In our sample, binaries with measured rotation periods have $\log L_X$ and $\log R_X$ ranges of from 28.19 to 30.99 and from -4.64 to -1.94, respectively. The fitting results with a two-piece power law are given in Table 3, with the slopes being -0.35 and -2.07 in the fast rotating region and slow rotating region, respectively. The knee point is logRo $= -1.32$. Meanwhile, some binaries could exhibit higher activity levels compared to single stars due to tidal interaction. There are 15 binaries with $\log R_X$ larger than -2.5. Among these sources, one was classified as RS CVn variables and six were classified as BY Dra variables, both of which are close binaries. The activity level affected by tidal interaction may explain the large scatter shown in the classical saturation region of the binary activity-rotation relation.

4. THE ULTRALUMINOUS SAMPLE

There is an Ultraluminous population of main-sequence stars with X-ray luminosities ranging from 10^{31} to 10^{33} erg/s, whose nature warrants investigation.

Although the luminosities of this population are close to the brightest YSOs and binaries, their R_X distribution spans from -3 to -1, significantly exceeding the distribution of YSOs and binaries. Furthermore, the spatial distribution of this population is much more scattered compared with YSOs and binaries (Figure 8), indicating they are different types of sources. Therefore, YSOs and binaries may have a minor contribution to the Ultraluminous population.

As discussed in Section 2.1 and 2.2, in our sample, approximately 10% of the optical counterparts to the X-ray sources may be incorrectly identified, due to the poor position accuracy of *ROSAT*. Previous studies have shown that galaxies and AGNs typically exhibit much higher X-ray to optical flux ratios than stars (e.g. Stocke et al. 1991; Hornschemeier et al. 2003). Recently, through comparing the optical counterparts identified by different methods, Freund et al. (2024) found a group of stars with distinctly high X-ray to bolometric flux ratios and argued that they are extragalactic

sources. Furthermore, it's reasonable to expect that galaxies and AGNs would have different spatial resolutions compared to stars, as shown in Figure 8. Besides, the portion of the Ultraluminous sources in the sample (i.e., $\sim 13\% = 258/2042$) roughly matches the false match rate. We further cross-matched the dwarf sample with the GLADE+ catalog (Dálya et al. 2022) using match radii of 10", 20", and 30", corresponding to 12, 68, and 146 targets, respectively. Therefore, we suspected that the Ultraluminous population could mainly consist of extragalactic sources.

5. X-RAY EMISSIONS AND HABITABLE ZONE

5.1. *mass loss rate induced by current X-ray emission*

The impact of stellar activity on stellar habitability is a hot topic. Generally, the habitable zone of a star is defined as the region in which liquid water can retain on a planet (e.g. Kasting et al. 1993; Kopparapu et al. 2013). However, the presence of liquid water is just one of the prerequisites for the generation of life. High energy emissions like UV and X-ray radiation could strongly affect the planetary habitability. UV emissions will not only influence the production of O_3 in the planetary atmosphere (Segura et al. 2003) but also trigger the formation of organic molecules (Powner et al. 2009). The UV habitable zone has been defined as the region in which a planet receives moderate UV radiation (Buccino et al. 2007; Spinelli et al. 2023).

Meanwhile, to establish a suitable temperature and pressure on a planet, the removal of its primordial H/He atmosphere is necessary, and a secondary atmosphere needs to be generated through processes such as volcanic activities to maintain liquid water (Kite & Barnett 2020; Swain et al. 2021). The high energy radiation of host stars plays a key role in the mass loss of the primordial atmosphere due to photoevaporation.

In this work, following the approaches of Murray-Clay et al. (2009) and Kubyshkina et al. (2020), we investigated the impact of X-ray emissions on the habitability of a planetary. First, for each single star in our sample, we calculated the inner boundary(d_{in}) and outer boundary(d_{out}) of the continuous habitable zone using the formular given by Kopparapu et al. (2014):

$$d = \left(\frac{L/L_\odot}{S_{\mathrm{eff}}}\right)^{0.5}\mathrm{AU}, \qquad (4)$$

where S_{eff} is calculated according to the coefficients from Kopparapu et al. (2014). Second, assuming there is a planet with one Earth mass ($M_{\mathrm{p}} = 1M_\oplus$) and one Earth radius ($R_{\mathrm{P}} = 1R_\oplus$) in the middle region of the continuous habitable zone ($\frac{d_{\mathrm{out}}+d_{\mathrm{in}}}{2}$), the mass loss rate $\dot{m}$ induced by X-ray emissions was estimated using the
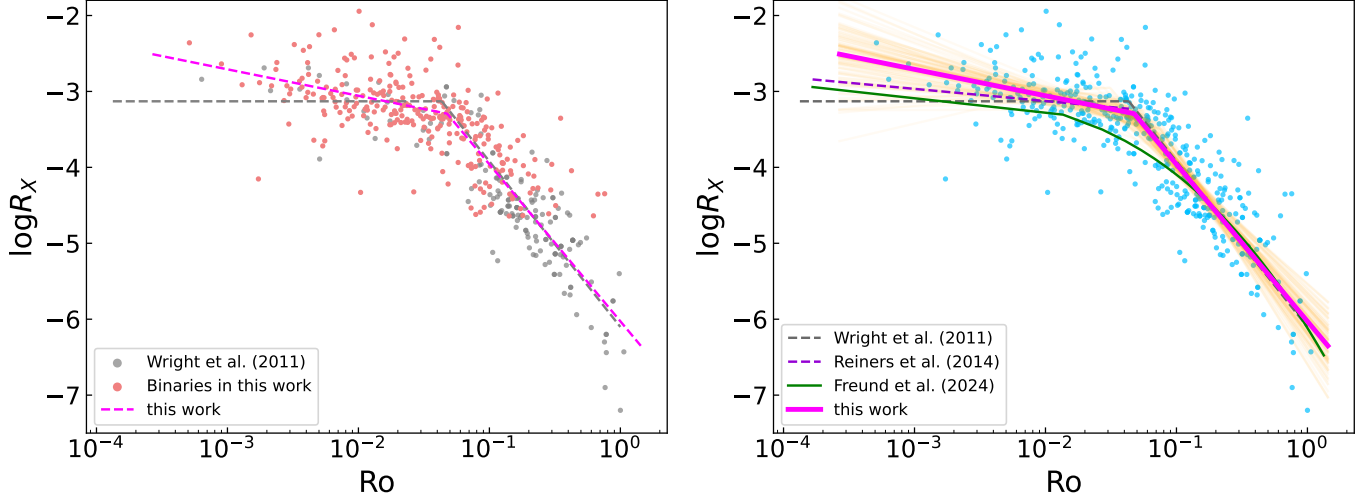
Figure 6. Panel (a): Activity-rotation relation of binaries. The grey and lightcoral dots are from Wright et al. (2011) and this work, respectively. Ro from Wright et al. (2011) are shifted by a factor of Ro/3. The magenta line is our best-fit result. Panel (b): Comparisons of activity-rotation relations from different studies. The shaded region shows 100 models extracted randomly from the posterior probability distribution.

formulae from Kubyshkina et al. (2020):

$$\dot{m} = \frac{\eta \pi F_{\mathrm{EUV}} R_{\mathrm{p}} R_{\mathrm{XUV}}^2}{G M_{\mathrm{p}} K}, \tag{5}$$

where F_{EUV} is the EUV flux at the distance of $\frac{d_{\mathrm{out}}+d_{\mathrm{in}}}{2}$. η is the parameter named heat efficiency and was set to be 0.15. The R_{XUV} is the effective absorption radius of XUV photons, which was defined by Chen & Rogers (2016):

$$R_{\mathrm{XUV}} = R_{\mathrm{p}} + H \ln \frac{P_{\mathrm{photo}}}{P_{\mathrm{XUV}}}. \tag{6}$$

Here H is the atmospheric scale height and P_{photo} is the pressure, whose values were adopted from Murray-Clay et al. (2009). P_{XUV} is the XUV absorption level. The factor K takes into account that the atmospheres only escape when it approaches the Roche lobe boundary, which was defined by Erkaev et al. (2007) as:

$$K = 1 - \frac{3}{2\xi} + \frac{1}{2\xi^3} \tag{7}$$

and

$$\xi = \left(\frac{M_{\mathrm{p}}}{3M_{\mathrm{s}}}\right)^{1/3} \frac{a}{R_{\mathrm{p}}}. \tag{8}$$

M_{s} is mass of host star and a is the semi-axis of planet, which was set to be $\frac{d_{\mathrm{out}}+d_{\mathrm{in}}}{2}$. The EUV flux was converted from our X-ray flux using the relation from Chadney et al. (2015):

$$\log F_{\mathrm{EUV}} = 2.63 + 0.58 \log F_{\mathrm{x}} \tag{9}$$

For detailed descriptions of above parameters we refer to Murray-Clay et al. (2009), Chen & Rogers (2016), and Kubyshkina et al. (2020).

If a planet keeps its primordial H/He atmosphere for a significant time, even though it resides in habitable zone, it won't be habitable (Owen & Mohanty 2016). A rocky Earth-like planet could accrete H/He envelope with a mass fraction of 0.1% to 1%, and such a scenario has been suggested by both theoretical and observational studies (e.g. Wolfgang & Lopez 2015; Rogers et al. 2011). Assuming there is a planet with a radius of $1R_{\oplus}$ and a primordial envelope fraction of 1% in the habitable zone of each star in our sample, we examined whether the X-ray-induced mass loss rate of planetary atmosphere is sufficient to significantly remove primordial envelope over 0.1 or 1 Giga years.

The mass loss rate to the primordial envelope within 0.1 Gyr and 1 Gyr are plotted by black and purple horizontal lines in Figure 9, respectively. Stars above the lines suggest their mass loss rates are high enough to remove the primordial envelope. Distances of the continuous habitable zones to M dwarfs are small, leading to much more significant atmospheric stripping due to X-ray emissions. Figure 9 suggests the primordial envelope of most of the M dwarfs could be removed within 1 Gyr, which is consistent with the results of Owen & Mohanty (2016).

5.2. mass loss rate corrected to young ages of stars

It's strange that our Sun lies below these lines, indicating an insufficient mass loss rate of the primordial envelope. One scenario is that the sun may have exhibited a much higher X-ray luminosity during the early formation stage of solar system (Güdel et al. 1997). Therefore,
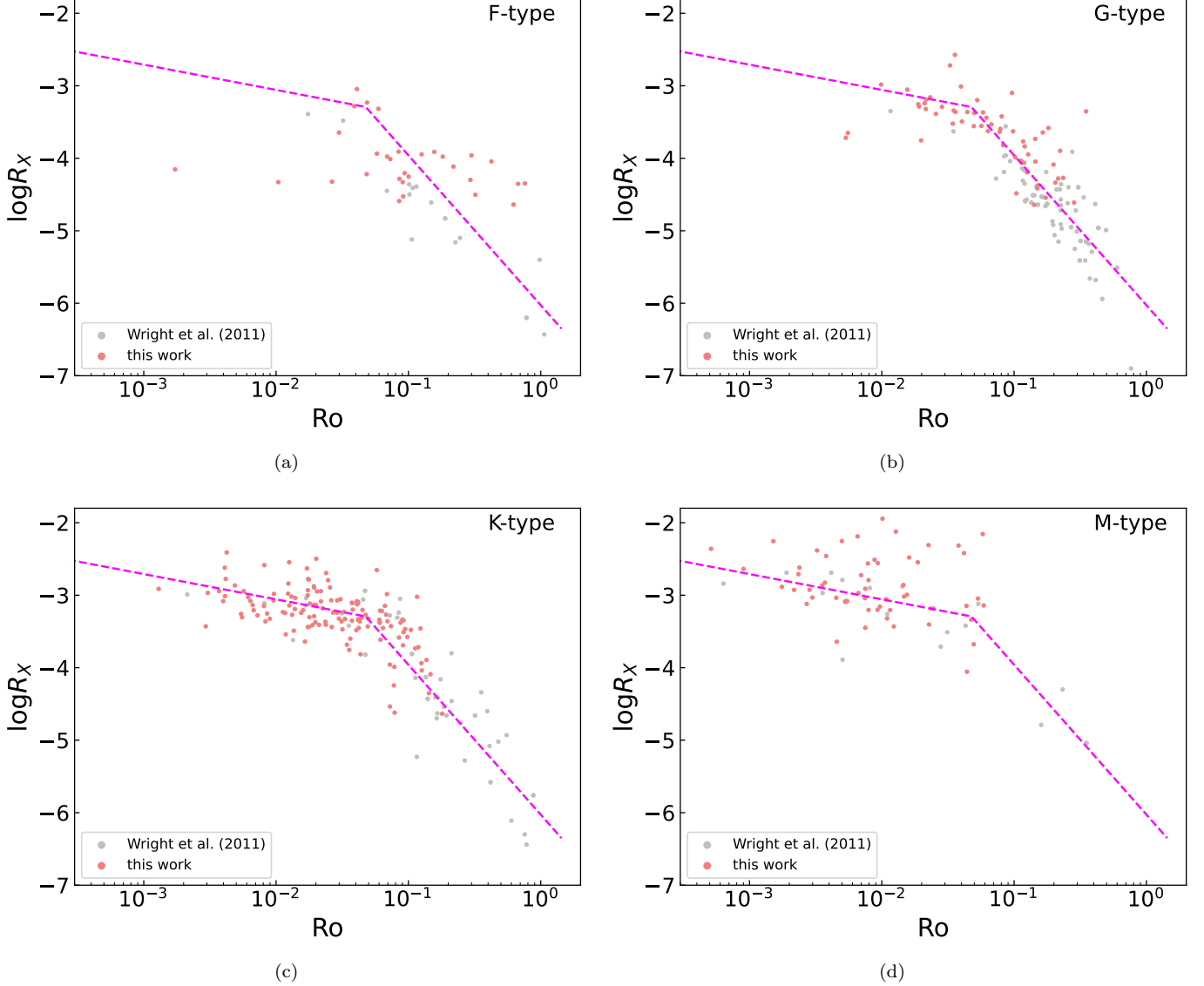
Figure 7. Activity-rotation of F-, G-, K-, and M-type binary stars, respectively. Binaries are categorized using the same criteria given in the caption of Figure 4. Magenta dashed line is the best-fit activity-rotation relation shown in Figure 6.

it would be worthwhile to correct the current X-ray luminosities of these stars to the values for their youth.

Previous studies have shown that the levels of stellar chromospheric and coronal activities would decrease as stars age (e.g. Mamajek & Hillenbrand 2008). Recently, Richey-Yowell et al. (2023) suggested the X-ray fluxes of K- and M-type stars can decrease by 100 to 1000 times when stars age from 10 Myr to 100 Myr. Therefore, the planetary atmosphere may suffer from a much stronger mass loss rate during the early stage of its host star.

Here we re-calculated the mass loss rate by using an X-ray luminosity corresponding to the stars' youth for our sample stars. The X-ray luminosity during the youth was assumed to be 500 times higher than the current

value. Figure 9 shows that with the re-calculated mass loss rate, most of the dwarfs could loss the primordial H/He envelope within 0.1 Giga year. Meanwhile, the X-ray emission from young Sun can strip away the Earth's primordial envelope with in 1 Giga year, thus enabling the development of life.

6. SUMMARY

In this work, utilizing the homogeneous *ROSAT* 2RXS all-sky X-ray catalog, together with LAMOST DR10, APOGEE DR16, Gaia eDR3 and various photometric sky surveys, we performed a comprehensive estimation of X-ray activities of late-type stars. Our sample includes a total of 2042 targets, among which 521 targets exhibit periodic modulation in light curves. The X-ray
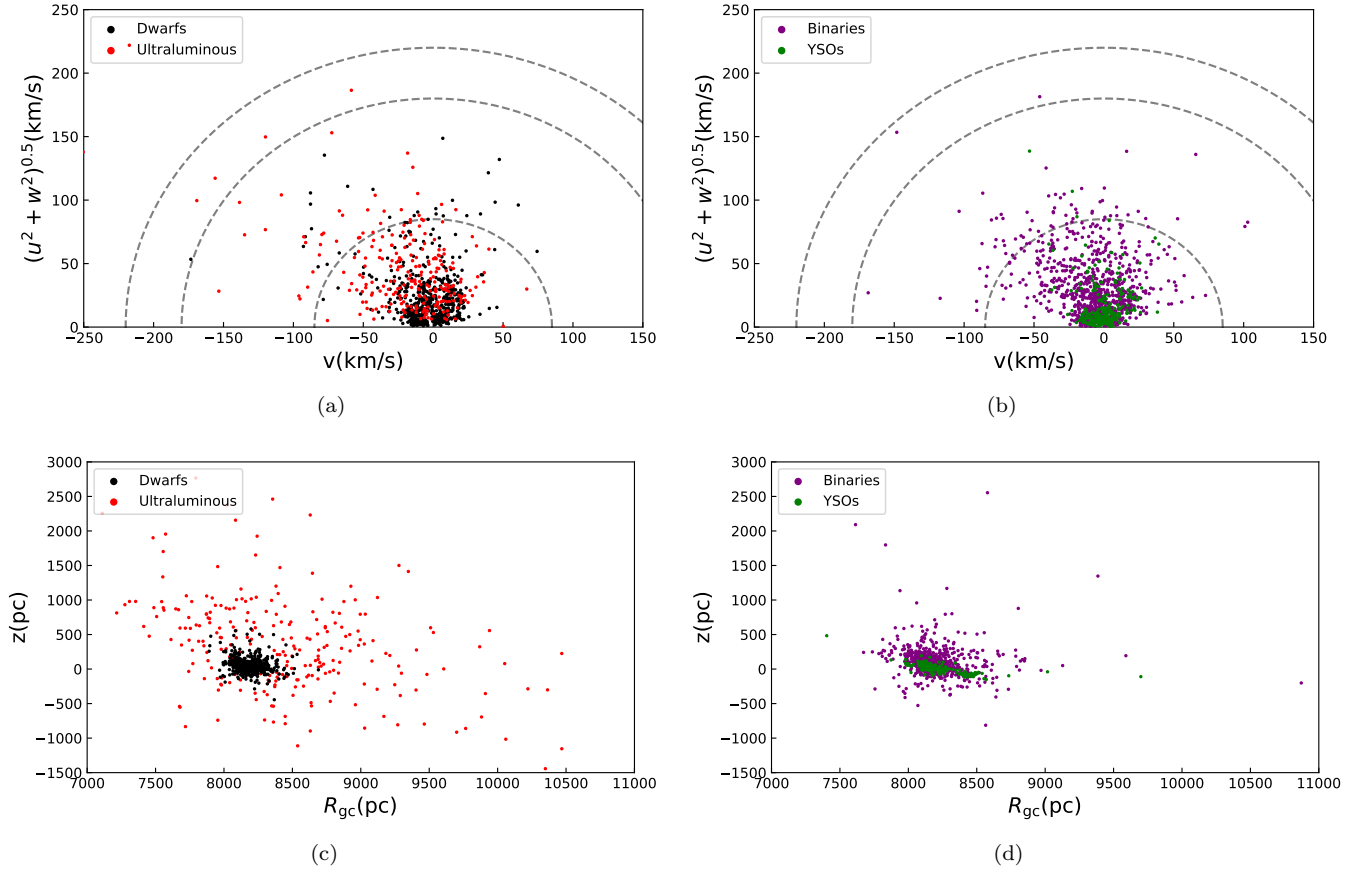
Figure 8. Panel (a): Toomre diagram of dwarfs and Ultraluminous sources. Panel (b): Toomre diagram of binaries and YSOs. (c) Galactic distribution of dwarfs and Ultraluminous sources. z is the vertical distance to the Galactic plane. R_{gc} is the radial distance to the Galactic center. (d) Galactic distribution of binaries and YSOs.

activity was quantified by the normalized X-ray flux R_X = f_X/f_{bol}. A detailed study of stellar activity-rotations was carried out for both single stars and binaries.

The overall activity-rotation relation can be roughly divided into two parts: a weak decay region and a rapid decay region, which can be referred to as the "D^2" model. In the fast-rotating regime, known as the saturated regime, our results show that there is still a weak dependence of R_X on Ro, suggesting a continued dependence of magnetic dynamo on stellar rotation. This contrasts with the conventional picture, which has shown a constant value of the activity index in this region.

However, detailed studies revealed some fine structures in the activity-rotation relation. In the extremely fast rotating regime, mainly composed of M stars, R_X was observed to decrease when stars rotate faster, a phenomenon named super-saturation, suggesting the decrease of the filling factors of active regions. On the other hand, in the extremely slow rotating region, a flat slope of R_X towards Ro was observed, mainly attributed to the scattering of F stars. This phenomenon may be caused by intrinsic variability of stellar activities (dur-

ing one stellar cycle) or different magnetic dynamos. We named the detailed activity-rotation relation, which can be divided into four parts, the "SD^{2}F" model.

Meanwhile, the activity-rotation relation of binaries is similar to that of single stars, suggesting the X-ray activities of binaries are dominated by the more active components. A slightly larger slope was observed in the fast rotating region for binaries, which can be attributed to the enhanced activity due to tidal interaction as binaries approach close separation. However, due to the limited sample size, no fine structure was found in the relation for binaries.

A group of dwarfs with very high L_X and R_X values were identified as the Ultraluminous sources. The size of the Ultraluminous sample roughly matches the false match rate of our sample. These sources exhibit a different spatial distribution compared to other stars, such as dwarfs, giants, and YSOs. Therefore, we suspected the Ultraluminous sample may mainly consist of extragalactic sources, such as AGN and galaxies.

Finally, we investigated the impacts of X-ray emissions to planetary atmosphere. By calculating the mass loss
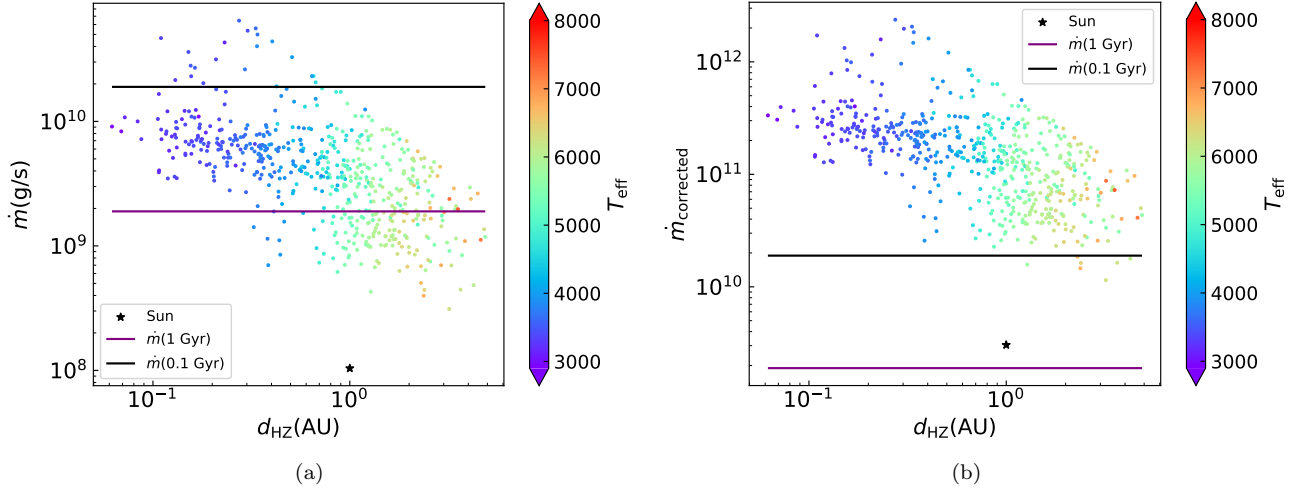
Figure 9. Panel (a): Mass loss rate of the planetary primordial atmosphere induced by X-ray emission. The mass loss rate within 0.1 and 1 Gyr are plotted with black and purple horizontal lines, respectively. Stars above the lines suggest they can remove the planetary primordial envelope within 0.1 or 1 Gyr. Different colors represent different effective temperatures. The Sun is donated by black star. Panel (b): Mass loss rate of planetary atmosphere induced by stellar X-ray emission which has been corrected to younger age.

rate of planetary primordial envelope in the continuous habitable zone, we found that most of the dwarfs can remove the primordial H/He envelope, which accounts for approximately 1% of the planetary mass, within one Giga year, especially for M-dwarfs whose habitable zones are close to host stars.

REFERENCES

Alfvén, H. 1947, MNRAS, 107, 211

Bailer-Jones, C. A. L., Rybizki, J., Fouesneau, M., Demleitner, M., & Andrae, R. 2021, AJ, 161, 147

Boller, T., Freyberg, M. J., Trümper, J., et al. 2016, A&A, 588, A103

Buccino, A. P., Lemarchand, G. A., & Mauas, P. J. D. 2007, Icarus, 192, 582

Chadney, J. M., Galand, M., Unruh, Y. C., Koskinen, T. T., & Sanz-Forcada, J. 2015, Icarus, 250, 357

Chahal, D., de Grijs, R., Kamath, D., & Chen, X. 2022, MNRAS, 514, 4932

Chen, H., & Rogers, L. A. 2016, ApJ, 831, 180

Chen, X., Wang, S., Deng, L., de Grijs, R., & Yang, M. 2018, ApJS, 237, 28

Chen, X., Wang, S., Deng, L., et al. 2020, ApJS, 249, 18

Christy, C. T., Jayasinghe, T., Stanek, K. Z., et al. 2022, PASP, 134, 024201

Cui, X.-Q., Zhao, Y.-H., Chu, Y.-Q., et al. 2012, Research in Astronomy and Astrophysics, 12, 1197

Dálya, G., Díaz, R., Bouchet, F. R., et al. 2022, MNRAS, 514, 1403

Drake, A. J., Graham, M. J., Djorgovski, S. G., et al. 2014, ApJS, 213, 9

El-Badry, K., Rix, H.-W., & Heintz, T. M. 2021, MNRAS, 506, 2269

Erkaev, N. V., Kulikov, Y. N., Lammer, H., et al. 2007, A&A, 472, 329

Favata, F., Giardino, G., Micela, G., Sciortino, S., & Damiani, F. 2003, A&A, 403, 187

Feigelson, E. D., Broos, P., Gaffney, James A., I., et al. 2002, ApJ, 574, 258

Feigelson, E. D., & Kriss, G. A. 1981, ApJL, 248, L35

Fitzpatrick, E. L. 1999, PASP, 111, 63

Flaccomio, E., Damiani, F., Micela, G., et al. 2003, ApJ, 582, 398

Foreman-Mackey, D. 2016, The Journal of Open Source Software, 1, 24. https://doi.org/10.21105/joss.00024

Foreman-Mackey, D., Hogg, D. W., Lang, D., & Goodman, J. 2013, PASP, 125, 306

Freund, S., Czesla, S., Predehl, P., et al. 2024, arXiv e-prints, arXiv:2401.17282

Gaia Collaboration, Brown, A. G. A., Vallenari, A., et al. 2021, A&A, 649, A1

Green, G. 2018, The Journal of Open Source Software, 3, 695

Green, G. M., Schlafly, E., Zucker, C., Speagle, J. S., & Finkbeiner, D. 2019, ApJ, 887, 93

Güdel, M., Guinan, E. F., & Skinner, S. L. 1997, ApJ, 483, 947

Han, H., Wang, S., Bai, Y., et al. 2023, ApJS, 264, 12

Hornschemeier, A. E., Bauer, F. E., Alexander, D. M., et al. 2003, AJ, 126, 575

Howard, E. L., Davenport, J. R. A., & Covey, K. R. 2022, Research Notes of the American Astronomical Society, 6, 96

James, D. J., Jardine, M. M., Jeffries, R. D., et al. 2000, MNRAS, 318, 1217

Jayasinghe, T., Stanek, K. Z., Kochanek, C. S., et al. 2020, MNRAS, 491, 13

Jenkins, J. M., Twicken, J. D., McCauliff, S., et al. 2016, in Society of Photo-Optical Instrumentation Engineers (SPIE) Conference Series, Vol. 9913, Software and Cyberinfrastructure for Astronomy IV, ed. G. Chiozzi & J. C. Guzman, 99133E

Johnstone, C. P., Bartel, M., & Güdel, M. 2021, A&A, 649, A96

Jönsson, H., Holtzman, J. A., Allende Prieto, C., et al. 2020, AJ, 160, 120

Kasting, J. F., Whitmire, D. P., & Reynolds, R. T. 1993, Icarus, 101, 108

Kite, E. S., & Barnett, M. N. 2020, Proceedings of the National Academy of Science, 117, 18264

Kopparapu, R. K., Ramirez, R. M., SchottelKotte, J., et al. 2014, ApJL, 787, L29

Kopparapu, R. K., Ramirez, R., Kasting, J. F., et al. 2013, ApJ, 765, 131

Kounkel, M., Covey, K. R., Stassun, K. G., et al. 2021, AJ, 162, 184

Kovalev, M., Chen, X., & Han, Z. 2022, MNRAS, 517, 356

Kubyshkina, D., Vidotto, A. A., Fossati, L., & Farrell, E. 2020, MNRAS, 499, 77

Lammer, H., Odert, P., Leitzinger, M., et al. 2009, A&A, 506, 399

Lehtinen, J. J., Spada, F., Käpylä, M. J., Olspert, N., & Käpylä, P. J. 2020, Nature Astronomy, 4, 658

Li, C.-q., Shi, J.-r., Yan, H.-l., et al. 2021, ApJS, 256, 31

Lomb, N. R. 1976, Ap&SS, 39, 447

Luo, A. L., Zhao, Y.-H., Zhao, G., et al. 2015, Research in Astronomy and Astrophysics, 15, 1095

Mamajek, E. E., & Hillenbrand, L. A. 2008, ApJ, 687, 1264

Marton, G., Tóth, L. V., Paladini, R., et al. 2016, MNRAS, 458, 3479

Marton, G., Ábrahám, P., Szegedi-Elek, E., et al. 2019, MNRAS, 487, 2522

Marton, G., Ábrahám, P., Rimoldini, L., et al. 2023, A&A, 674, A21

MAST Team. 2021, TESS Light Curves - All Sectors, STScI/MAST, doi:10.17909/T9-NMC8-F686

McQuillan, A., Aigrain, S., & Mazeh, T. 2013, MNRAS, 432, 1203

McQuillan, A., Mazeh, T., & Aigrain, S. 2014, ApJS, 211, 24

Mittag, M., Schmitt, J. H. M. M., & Schröder, K. P. 2018, A&A, 618, A48

Morton, T. D. 2015, isochrones: Stellar model grid package, Astrophysics Source Code Library, record ascl:1503.010, , , ascl:1503.010

Motch, C., Warwick, R., Cropper, M. S., et al. 2010, A&A, 523, A92

Murray-Clay, R. A., Chiang, E. I., & Murray, N. 2009, ApJ, 693, 23

Newton, E. R., Irwin, J., Charbonneau, D., et al. 2017, ApJ, 834, 85

Noyes, R. W., Hartmann, L. W., Baliunas, S. L., Duncan, D. K., & Vaughan, A. H. 1984, ApJ, 279, 763

Owen, J. E., & Mohanty, S. 2016, MNRAS, 459, 4088

Pallavicini, R., Golub, L., Rosner, R., et al. 1981, ApJ, 248, 279

Parker, E. N. 1955, ApJ, 122, 293

—. 1988, ApJ, 330, 474

Pizzocaro, D., Stelzer, B., Poretti, E., et al. 2019, A&A, 628, A41

Pizzolato, N., Maggio, A., Micela, G., Sciortino, S., & Ventura, P. 2003, A&A, 397, 147

Powner, M. W., Gerland, B., & Sutherland, J. D. 2009, Nature, 459, 239

Preibisch, T., & Feigelson, E. D. 2005, ApJS, 160, 390

Prša, A., Kochoska, A., Conroy, K. E., et al. 2022, ApJS, 258, 16

Randich, S., Schmitt, J. H. M. M., Prosser, C. F., & Stauffer, J. R. 1996, A&A, 305, 785

Reiners, A., Schüssler, M., & Passegger, V. M. 2014, ApJ, 794, 144

Ren, J. J., Rebassa-Mansergas, A., Parsons, S. G., et al. 2018, MNRAS, 477, 4641

Ren, J. J., Raddi, R., Rebassa-Mansergas, A., et al. 2020, ApJ, 905, 38

Richey-Yowell, T., Shkolnik, E. L., Schneider, A. C., et al. 2023, ApJ, 951, 44

Ricker, G. R., Winn, J. N., Vanderspek, R., et al. 2015, Journal of Astronomical Telescopes, Instruments, and Systems, 1, 014003

Rimoldini, L., Holl, B., Gavras, P., et al. 2023, A&A, 674, A14

Rogers, L. A., Bodenheimer, P., Lissauer, J. J., & Seager, S. 2011, ApJ, 738, 59

Salvato, M., Buchner, J., Budavári, T., et al. 2018, MNRAS, 473, 4937

Samus', N. N., Kazarovets, E. V., Durlevich, O. V., Kireeva, N. N., & Pastukhova, E. N. 2017, Astronomy Reports, 61, 80

Santos, A. R. G., Breton, S. N., Mathur, S., & García, R. A. 2021, ApJS, 255, 17

Santos, A. R. G., García, R. A., Mathur, S., et al. 2019, ApJS, 244, 21

Scargle, J. D. 1982, ApJ, 263, 835

Schlegel, D. J., Finkbeiner, D. P., & Davis, M. 1998, ApJ, 500, 525

Segura, A., Krelove, K., Kasting, J. F., et al. 2003, Astrobiology, 3, 689

Soszyński, I., Pawlak, M., Pietrukowicz, P., et al. 2016, AcA, 66, 405

Spada, F., Demarque, P., Kim, Y. C., Boyajian, T. S., & Brewer, J. M. 2017, ApJ, 838, 161

Spinelli, R., Borsa, F., Ghirlanda, G., Ghisellini, G., & Haardt, F. 2023, MNRAS, 522, 1411

Stassun, K. G., Oelkers, R. J., Paegert, M., et al. 2019, AJ, 158, 138

Stauffer, J. R., Hartmann, L. W., Prosser, C. F., et al. 1997, ApJ, 479, 776

Stępień, K., Schmitt, J. H. M. M., & Voges, W. 2001, A&A, 370, 157

Stocke, J. T., Morris, S. L., Gioia, I. M., et al. 1991, ApJS, 76, 813

Swain, M. R., Estrela, R., Roudier, G. M., et al. 2021, AJ, 161, 213

Truemper, J. 1982, Advances in Space Research, 2, 241

Vaiana, G. S., Cassinelli, J. P., Fabbiano, G., et al. 1981, ApJ, 245, 163

van Ballegooijen, A. A., Asgari-Targhi, M., Cranmer, S. R., & DeLuca, E. E. 2011, ApJ, 736, 3

Voges, W., Aschenbach, B., Boller, T., et al. 1999, A&A, 349, 389

Wang, S., Bai, Y., He, L., & Liu, J. 2020, ApJ, 902, 114

Wang, S., Liu, J., Qiu, Y., et al. 2016, ApJS, 224, 40

Wei, X. 2022, ApJ, 926, 40

Wolfgang, A., & Lopez, E. 2015, ApJ, 806, 183

Wright, N. J., Drake, J. J., Mamajek, E. E., & Henry, G. W. 2011, ApJ, 743, 48

Wright, N. J., Newton, E. R., Williams, P. K. G., Drake, J. J., & Yadav, R. K. 2018, MNRAS, 479, 2351

Zhang, B., Jing, Y.-J., Yang, F., et al. 2022, ApJS, 258, 26

Zhu, H., Tian, W., Li, A., & Zhang, M. 2017, MNRAS, 471, 3494

APPENDIX

A. R_X COMPARISONS BETWEEN THIS WORK AND PREVIOUS STUDIES

Figure A1 shows the comparison of R_X between this work and Wright et al. (2011). Figure A2 shows the comparison of R_X between Freund et al. (2024) and other studies.
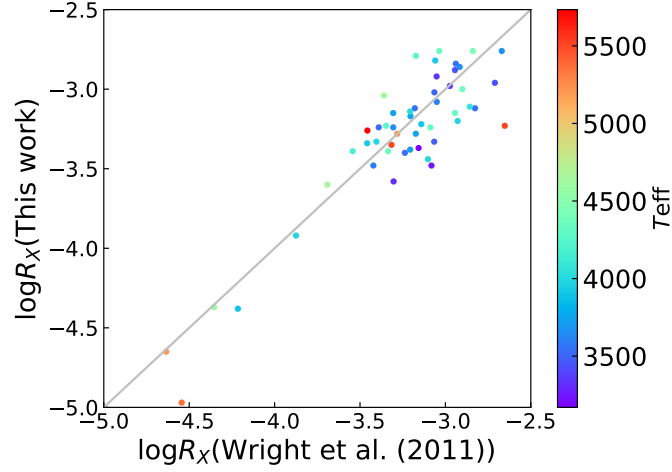

Figure A1. Comparison of R_X of common targets between this work and Wright et al. (2011). Different colors represent different effective temperatures.
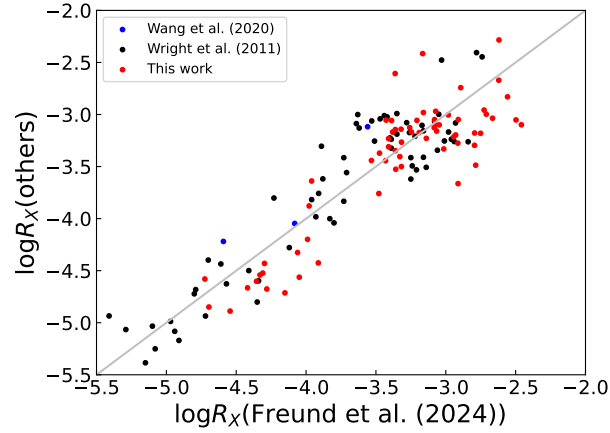

Figure A2. Comparison of R_X of common targets between various literature and Freund et al. (2024). Different colors represent sources from different literature.

B. MCMC RESULTS OF THE FITS TO ACTIVITY-ROTATION RELATIONS

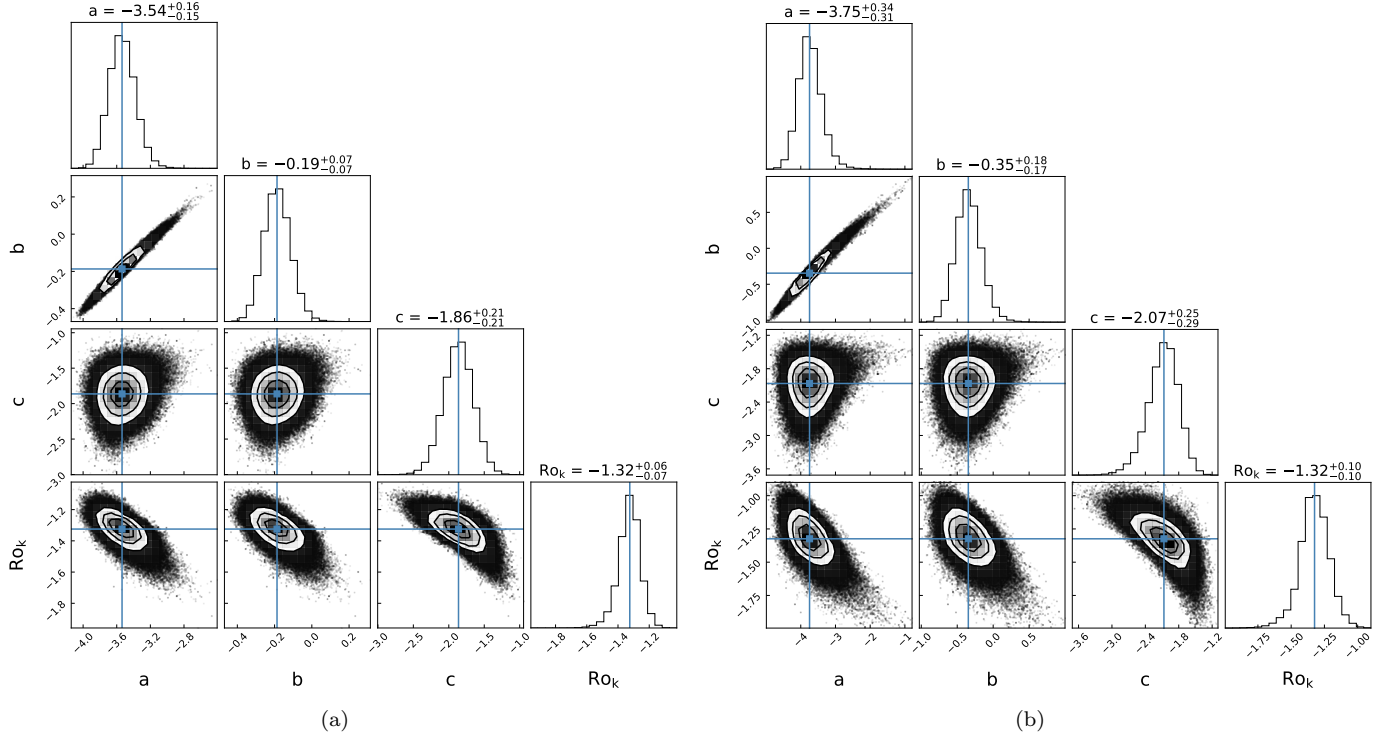Figure B1 shows the posterior distributions of parameters of the best-fit piece-wise power laws.

Figure B1. Panel (a): posterior distributions of parameters of the piece-wise power law for single stars. Panel (b): posterior distributions of parameters of the piece-wise power law for binaries

.